








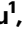

Optomechanical sensor network with fiber Bragg gratings

Received: 9 September 2024

Accepted: 4 November 2025

Published online: 02 December 2025

 Check for updates

Shiwei Yang ^{1,3}, Qiang Zhang ^{1,2,3} , Linrun Yang ^{1,3}, Hanghua Liu¹,
Quansen Wang¹, Pengfei Zhang ^{1,2}, Heng Shen ^{1,2}  & Yongmin Li ^{1,2} 

Sensor networks are indispensable for diverse engineering applications and cutting-edge scientific research. Recent advances in cavity optomechanics have enabled progress in ultrasensitive sensing. Crucially, the resonant enhancement of optical and mechanical responses enables highly sensitive detection of small perturbations, making it a promising candidate for next-generation ultrasensitive sensor networks. However, the intrinsic limitations of existing optomechanical sensors—such as fiber-optic integration and polarization-dependent response—have hindered progress in this field. Here, we demonstrate a kilometer-scale optomechanical sensor network, integrating multiple fiber-optic optomechanical sensors into a standard single-mode fiber. Leveraging commercially available fiber Bragg gratings, we achieve robust, low-loss, low-noise, and polarization-insensitive coupling with light sources. Within this network, which incorporates both scalar and vector magnetometers, we illustrate the network operation by resolving the spatial variations in the magnetic field under a magnetically unshielded environment with the ambient temperature and pressure. Our work advances the practical application of cavity optomechanics in ultrasensitive sensor networks.

Sensor networks exploit multiple sensors distributed across the area of interest to obtain the comprehensive information of the targets, playing essential roles in a variety of applications ranging from internet of things¹, smart cities², oil and gas industry³, seafloor faults and ocean dynamics⁴, to earthquake and volcano dynamic detection^{5,6}. Of particular importance is the key building block of the network, the sensor, which should fulfill the requirement of high-sensitivity, robustness, scalability, and multiplexing.

In recent years, cavity optomechanics has emerged as a platform for single-point ultrasensitive sensing^{7–48}, enabling optical detection of diverse physical quantities including small forces^{15–19}, displacements^{20–23}, rotations^{24–26}, vibrations^{27–31}, ultrasounds^{32–34}, radio waves^{35–39}, magnetic fields^{40–46}, and other quantities^{47,48}. Recent work has demonstrated the operation of a sensing network on a sub-millimeter chip⁴⁹, where three whispering gallery mode sensors were coupled via a bus waveguide. However, realizing a kilometer-scale

optomechanical sensor network remains challenging, as it requires a cascaded integration of all sensors via standard single-mode fiber (SMF) while maintaining polarization immunity against random birefringence effects that accumulate over long distances⁵⁰.

In this work, we demonstrate a kilometer-scale optomechanical sensor network by cascading multiple fiber-optic optomechanical sensors into a standard SMF. By incorporating fiber mechanical resonator (MR) and phase-shifted fiber Bragg grating (PFBG) into optomechanical systems, we achieve robust, low-loss, and polarization-insensitive coupling to light sources. Then, as proof-of-concept we apply this sensor network for the detection of magnetic fields. Both achieved peak DC magnetic-field sensitivity of 8.73 pm/Gs (the resonant wavelength shift of the PFBG per unit Gauss), and the peak AC magnetic-field sensitivity of 537 fTHz^{1/2} are better than the best values reached with existing optomechanical magnetometers (7.57 pm/Gs in ref. 47 and 620 fTHz^{1/2} in ref. 44). Furthermore, we demonstrate a

¹State Key Laboratory of Quantum Optics Technologies and Devices, Institute of Opto-Electronics, Shanxi University, Taiyuan, China. ²Collaborative Innovation Center of Extreme Optics, Shanxi University, Taiyuan, China. ³These authors contributed equally: Shiwei Yang, Qiang Zhang, Linrun Yang.

 e-mail: qzhang@sxu.edu.cn; hengshen@sxu.edu.cn; yongmin@sxu.edu.cn

kilometer-scale optomechanical magnetometer network capable of real-time monitoring of spatial magnetic field variations from moving targets. The network integrates both scalar and vector magnetometers to provide complete field characterization.

Results

Principle of operation

Figure 1a illustrates the schematic of an optomechanical sensor network, where multiple sensors are integrated into a standard SMF for quasi-distributed sensing. In this architecture, both DC and AC magnetic field can be detected. Concretely, we obtain the response to DC magnetic field by monitoring the reflective spectrum of the sensor network, wherein a broadband source (BBS) and an optical spectrum analyzer (OSA) are used. On the other hand, to probe the AC magnetic field, lights with different wavelengths are coupled into the sensor network by a wavelength division multiplexer (WDM) and a fiber circulator. The reflective light is demodulated using a WDM and photodetectors. We stress that this system works in a magnetically unshielded environment with ambient temperature and pressure.

As the key element, the optomechanical sensor consists of a clamped-clamped fiber MR (blue) and a functional support (black) as shown in Fig. 1b. And Fig. 1c displays the typical photograph of the FOMM. Here, the fiber MR is fabricated by sequentially inserting a commercial standard PFBG (typical reflective spectrum is presented in Fig. 1d) into two silica capillaries and filling the gap with UV glue. The abrupt junction between the PFBG and silica capillaries induces an acoustical mismatched impedance, confining the phonons into the PFBG to form a high-Q mechanical resonator⁵¹.

As a demonstration of detecting the magnetic field, we further use a cuboid Terfenol-D rod as the functional support (in Fig. 1b, c) to respond to the ambient magnetic field. Figure 1e shows the mode shapes of the fiber MR and the Terfenol-D MR. Consequently, when an ambient magnetic field is applied to the FOMM, the Terfenol-D rod generates the associated deformation and thus changes the length and grating period of the fiber MR. By interrogating the reflection of the

PFBG determined by the grating period, the ambient magnetic field could be measured in real time. Intriguingly, a large optomechanical coupling coefficient is promised by the coaxial coupling between motion of the Terfenol-D rod and the PFBG.

To improve the sensitivity, a mechanism of deformation transfer is used to amplify the strain of the fiber MR from the deformation of the Terfenol-D rod with a deformation transfer ratio (D_{TR}) of $D_{TR} = L_1/L_2$. Here the deformation of the Terfenol-D rod with a length of L_1 is transferred to fiber MR with a length of L_2 , as shown in Fig. 1b. Therefore, by increasing L_1 and decreasing L_2 , one can achieve a larger value of D_{TR} and thus improved the sensitivity.

Building upon such scalable and fiber-compatible magnetometers, a sensor network is constructed by simply injecting probe light into the sensor network through a fiber-optic circulator. This thus provides a simple, robust, low-noise and low-loss coupling approach. Meanwhile, the PFBG is isotropic for the polarizations of probe light as shown in Fig. S3 (in the Supplementary Information), suppressing the influence of optical polarization fluctuations from random birefringence in SMF, especially for long-distance networks. Furthermore, using commercially available fiber Bragg gratings and WDMs promises a practical pre-distributed optomechanical sensing network.

Response to DC magnetic fields

We first investigate the system response to the DC magnetic fields. A broadband light source and an optical spectrum analyzer are used to measure the reflective spectrum shifts of the FOMMs with different D_{TR} as shown in Fig. 1a. The resonant wavelength shift $\Delta\lambda$ resulted from the applied DC magnetic field \mathbf{B} is given by ref. 52

$$\Delta\lambda(\mathbf{B}) = 0.74\lambda_c\alpha\mathbf{B}D_{TR} \quad (1)$$

where λ_c is the dip wavelength of the PFBG in absence of the magnetic fields and α is magnetostrictive coefficient of the Terfenol-D rod.

In our experiment, the DC magnetic field is generated using an 18-mm-diameter coil, which is calibrated with a commercial magnetic

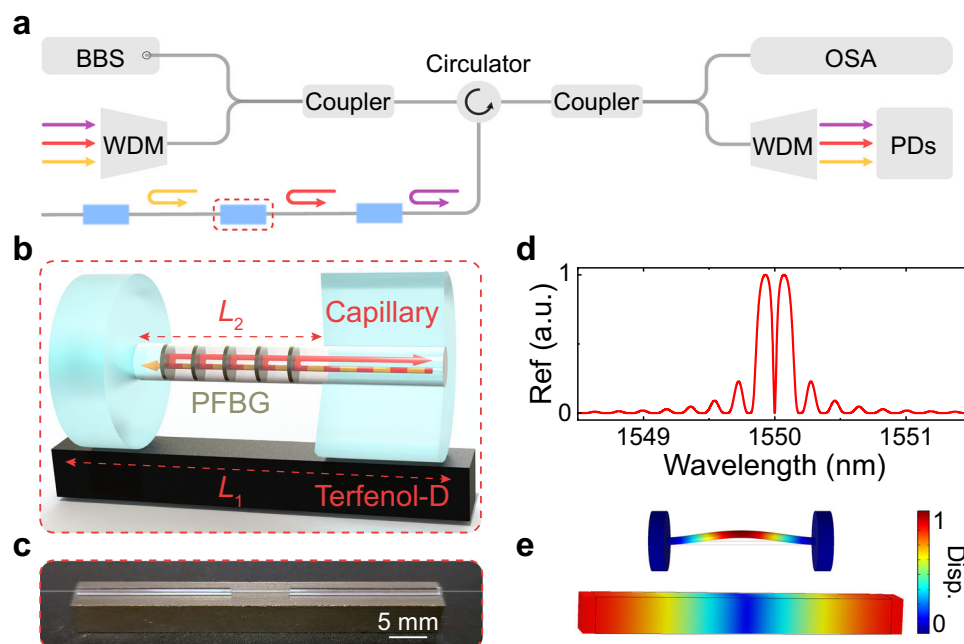


Fig. 1 | Optomechanical sensor network. **a** Experimental apparatus of the sensor network. **b** Schematic diagram of the FOMM. The PFBG works as an optical cavity to readout the motion state of the fiber MR. When light with different wavelengths (colored arrow from right to left) is injected into the PFBG, the resonant light (red arrow) is reflected and the others pass through the PFBG. **c** Photograph of the

FOMM. **d** Normalized reflective spectrum of a representative PFBG. **e** Finite-element simulations of mode shapes of the fiber MR and Terfenol-D MR. Disp. mechanical displacement, BBS broadband source, OSA optical spectrum analyzer, WDM wavelength division multiplexer, PDs photodetectors.

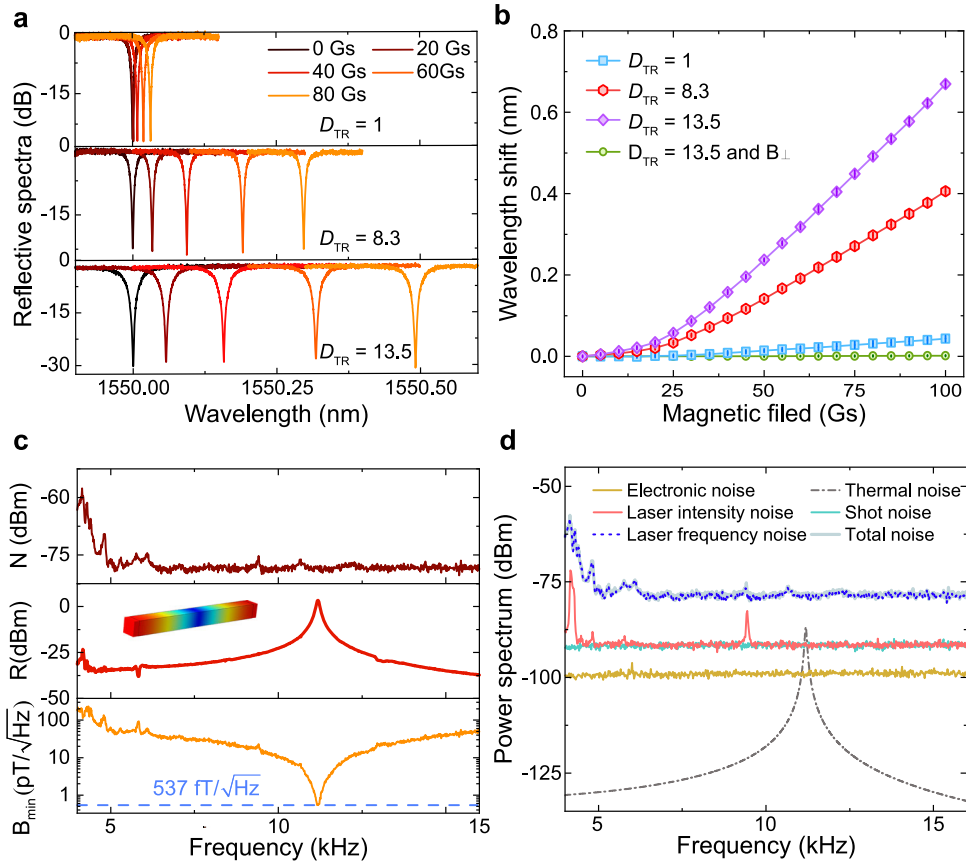


Fig. 2 | Response of the FOMMs to DC and AC magnetic fields. a Reflective spectrum shifts of the FOMMs with different D_{TR} of 1, 8.3, and 13.5 as a function of DC magnetic fields. **b** Resonant wavelength shifts of the three FOMMs as a function of coaxial and orthogonal DC magnetic fields. **c** Noise power spectrum $N(\omega)$ of the FOMM without magnetic excitation (upper), response $R(\omega)$ to frequency scanning

magnetic excitation (middle), and resolution B_{min} as a function of frequency (bottom). Inset: Finite-element modeling of mechanical resonant eigenmode of the Terfenol-D rod. **d** Analysis of optical noise power spectrum. Resolution bandwidth (RBW) of the power spectra is 10 Hz.

sensor. Figure 2a shows the reflective spectra of the FOMMs with different D_{TR} under varying DC magnetic fields. We observe that the resonant dip of the PFBG shifts to the long wavelength region (red-shift) as the DC magnetic fields increase. The wavelength shift is proportional to the D_{TR} and ambient magnetic fields. The peak sensitivity is 8.73 pm/Gs (the resonant wavelength shift of the PFBG per unit Gauss) for the FOMM with an D_{TR} of 13.5, which is in good agreement with the theoretical values ($\lambda_c = 1550$ nm and $\alpha = 0.564$ ppm/Gs). The corresponding optomechanical coupling constant g_{OM} is $2\pi \times 38.7$ MHz/nm, where $g_{OM} = \partial\omega_c/\partial x$ is defined as the resonant frequency shift per unit displacement.

In parallel, direction of magnetic field is another key parameter for measuring the ambient magnetic fields. In Fig. 2b, the green curve represents the response of the FOMM ($D_{TR} = 13.5$) to a magnetic field orthogonal to the axis of the Terfenol-D rod. The corresponding sensitivity is 0.01 pm/Gs, which is about one thousandth of that of the FOMM to a magnetic field coaxial with the Terfenol-D rod. Therefore, the FOMM realizes one-dimensional directional magnetic-field measurement, overcoming the restrict of direction-insensitivity in reported optomechanical magnetometers and providing a potential way for detecting three-dimensional vector magnetic fields.

Response to AC magnetic fields

To examine the response of the FOMM to AC magnetic fields, a probe light from a tunable laser is coupled into the FOMM to monitor the deformation of the fiber MR using the dispersive coupling mechanism, where the wavelength of the probe light is slightly detuned from the optical resonant dip. The reflective optical power with AC magnetic

field excitations is given by

$$P(\omega) = \eta P_{in} + \Delta k \quad (2)$$

where η and P_{in} are the reflectivity of the PFBG at the wavelength of the probe light and the input power of the probe light, and k is the slope of the reflective spectrum of the PFBG and is achieved from the derivation of Lorentzian function

$$k(\Delta) = \frac{8\omega_{PFBG}^2 P_0 (R_{max} - R_{min}) \Delta}{(4\Delta^2 + \omega_{PFBG}^2)^2} \quad (3)$$

where $\Delta = \lambda_p - \lambda_c$ is the laser-cavity detuning, ω_{PFBG} is the FWHM of the PFBG, P_0 is light power, R_{max} is the maximum reflectivity of the PFBG, and R_{min} is the reflectivity of the PFBG at optical resonant dip. When the frequency of the probe light is detuned by $\Delta = \pm\omega_{PFBG}/12^{1/2}$, the slope k is maximized

$$k(\Delta = \pm\omega_{PFBG}/2\sqrt{3}) = \frac{3\sqrt{3}P_0(R_{max} - R_{min})}{4\omega_{PFBG}} \quad (4)$$

The Response $R(\omega)$ in unit of dBm under AC magnetic excitation could be expressed as²⁸

$$R(\omega) = 10 \log \left(\frac{(g\gamma\Delta k)^2}{Z} 1000 \right) \quad (5)$$

where g and γ are the conversion gain and rate of the photodetector, and Z is 50 Ω . For AC magnetic-field measurement, the mechanical resonances need to be considered, and the resonant wavelength shift $\Delta\lambda = 0.74\lambda_p\alpha D_{TR}\omega_{TD}^2\chi(\omega)$, where ω_{TD} and $\chi(\omega)$ are the resonant frequency and mechanical susceptibility of the Terfenol-D MR. Finally, the AC magnetic-field sensitivity could be obtained as⁴¹

$$B_{\min}(\omega) = \frac{B_{\text{ref}}}{\sqrt{\text{SNR}(\omega) \times \text{RBW}}} \quad (6)$$

where the signal-to-noise ratio (SNR) is the ratio of the response $R(\omega)$ to the noise floor.

Figure 2c and d depicts a typical measurement at ambient temperature and pressure. Concretely, Fig. 2c shows the noise power spectrum $N(\omega)$ (upper panel) and the response $R(\omega)$ (middle panel) of the FOMM with a D_{TR} of 5.1, where the amplitude of AC magnetic-field B_{ref} keeps constant at 24 nT, and the resolution bandwidth (RBW) of the spectrum analyzer is 10 Hz. The response peak in Fig. 2c (middle panel) locates at the position of the fundamental stretching mode of the Terfenol-D rod with a mechanical quality factor of 180. Experimental results show that the peak AC sensitivity is 537 fTHz^{1/2} at 11.188 kHz, as shown in Fig. 2c (bottom panel). The corresponding continuous 3-dB bandwidth⁴³ is 62 Hz. We would like to emphasize that the sensitivity varies considerably at the resonance frequencies of different mechanical eigenmodes. In particular, the response is proportional to the mechanical susceptibility of the MR $\chi(\omega) = (\omega_m^2 - \omega^2 - i\Gamma)^{-1}$ with the (energy) damping rate of mechanical mode Γ_m ⁷. By introducing the mechanical quality factor $Q_m = \omega_m / \Gamma_m$, it is found that the resonant response of the FOMM (i.e., optimal sensitivity) is proportional to $\chi(\omega) = i / (\Gamma_m\omega_m) = iQ_m / \omega_m^2$, and the continuous 3-dB bandwidth as defined by ref. 40 is determined by Γ_m . Given the resonance frequency ω_m , this naturally leads to a tradeoff between response and bandwidth. In addition, Terfenol-D mechanical resonator supports many mechanical modes ranging from 11 kHz to hundreds of kHz, during which our optomechanical sensor can detect magnetic fields. And in practice, most of the applications of magnetic field detection focus on the frequency range of DC to hundreds of kHz⁵³.

To fully characterize the performance of the optomechanical sensor, we measure all the classical noise, such as detector electronic noise, laser intensity and frequency noise and shot noise, while calculating the thermal noise of mechanical oscillator with a RBW of 10 Hz. The results are plotted as Fig. 2d, and the derivation of the thermal noise is presented in the Supplementary Information S4. It is observed that the measured total noise is dominated by the laser frequency noise. The thermal noise of the stretching eigenmode of the Terfenol-D MR is beneath the noise floor, indicating that the precision of this sensor could be improved by decreasing the laser frequency noise.

Tunable resonant responses

In practice, broadband ultrasensitive measurement is challenging for the reported optomechanical magnetometers. However, our device addresses this issue by employing a bias magnetic field to adjust the resonant frequency of the Terfenol-D MR. For the FOMM with a D_{TR} of 9.3, when the bias magnetic field increases from 0 Gs to 200 Gs, the resonant frequency of the Terfenol-D MR decreases about 1.3 kHz in Fig. 3a, b. The associated response and sensitivity under different bias magnetic fields are illustrated in Fig. 3a, c. In accordance with Eq. 5 and Eq. 6, the variation of the sensitivity results from the changes of the magnetostrictive coefficient α of the Terfenol-D MR and the Q_m of the Terfenol-D MR. Specifically, as shown in Fig. 3d, when the bias magnetic field increases from 0 Gs to 50 Gs, α increases gradually and then reaches the saturation afterwards. However, the Q_m decreases rapidly from 146 to 9 as the bias magnetic field increases from 0 Gs to

100 Gs and becomes constant when the bias magnetic field increases further. Similar performances of the Terfenol-D material have been observed in related works^{54,55}. In fact, the resonant frequency of the fiber MR could be also changed by the bias magnetic field. Figure 3b shows that the resonant frequency of fundamental flexural mode of the fiber MR increases by 5.63 kHz as the bias magnetic field increases from 0 Gs to 200 Gs. However, as shown in Fig. 3a, the mechanical mode of the Terfenol-D MR presents higher response and better sensitivity with respect to the fiber MR. Therefore, the peak AC sensitivities in this work are obtained at the resonant frequency of the Terfenol-D MR.

Optomechanical sensor network

We demonstrate a kilometer-scale optomechanical sensor network, and the associated results are illustrated in Fig. 4. Specifically, we report the successful network operation by resolving the spatial variations in the magnetic field, where a moving coil generating a constant AC magnetic field passes through all the sensors subsequently.

As shown in Fig. 4a, b, in this network nine fiber-optic optomechanical sensors (labeled Sensor 1–9) are deployed. Sensors 1–3 are arranged in parallel with a 25 mm separation, forming a scalar magnetometer (FOMMA) aligned with the applied magnetic field. Sensor 4–6 oriented orthogonally to each other constitute a vector magnetometer (FOMMB), with Sensor 6 parallel to Sensors 1–3. Another vector magnetometer (FOMMC) consists of Sensors 7–9, also orthogonally arranged but inclined at 66°, 35°, and 66° relative to the magnetic field. All units (FOMMA–C) are interconnected via a one-kilometer single-mode optical fiber, as depicted in Fig. 4b.

When the coil with a 6.4 μT AC magnetic field at the resonance frequency of the Terfenol-D rod moves from right to left, the sensor network responds to the vector magnetic field in real time. Figure 4c shows the measured results. As the coil passes FOMMC, all three sensors (7, 8, and 9) exhibit clear responses, with amplitudes matching the theoretical predictions. When the coil moves close to FOMMB, only Sensor-6 responds significantly, while the others remain negligible due to their orthogonal alignment with the coil's field. These results demonstrate the system's capability for vector magnetic field measurement. When the coil approaches FOMMA, the three sensors show position-dependent responses, enabling coil localization through signal demodulation. By strategically deploying these optomechanical sensors, the sensing network can monitor magnetic-field variations at multiple positions and track the motion of magnetic objects. This technology holds promise for applications such as power transmission systems, antisubmarine operations, smart cities, and the Internet of Things.

Discussion

We report a unique cavity optomechanical sensor network, integrating the advantages of optomechanical ultrasensitive sensing mechanisms and advanced optical fiber sensing technologies. This system achieves robust, low-loss optical coupling, enabling practical deployment of cavity optomechanics in real-world applications. Moreover, FBGs are insensitive to polarization fluctuations and compatible with mature optical fiber multiplexing technologies, providing a promising candidate for long-distance sensing networks.

As a proof-of-concept, we demonstrate a kilometer-scale optomechanical magnetometer network, achieving unprecedented DC and AC sensitivities at a magnetically unshielded ambient temperature and pressure. This network holds great potential for geomagnetic anomalies, space exploration missions, and mineral exploration. This sensing scheme could also be employed to measure strains, vibrations, and acoustic waves by choosing appropriate support, making this platform particularly promising for the oil and gas industry, seafloor faults and ocean dynamics, and earthquake and volcano dynamic detection.

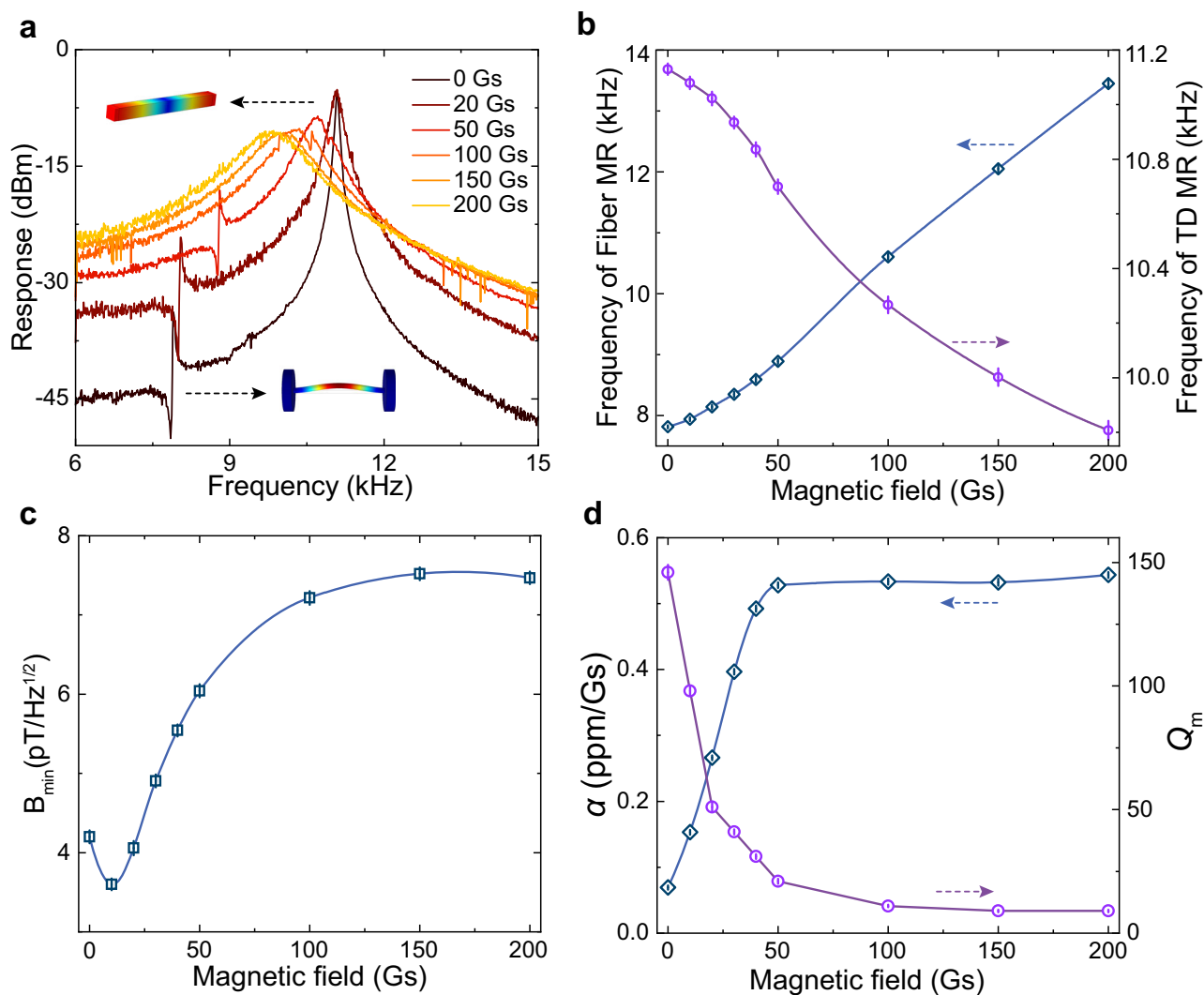


Fig. 3 | Tunable resonant responses. **a** Responses of the FOMM under different bias magnetic fields. Inset: Finite-element modeling of mechanical resonant eigenmodes of the Terfenol-D and fiber MRs. **b** Resonant frequency shifts of the

Terfenol-D and fiber MRs as a function of bias magnetic fields. **c** AC sensitivity B_{\min} under different bias magnetic fields. **d** α and Q_m as a function of bias magnetic fields.

The DC magnetic-field sensitivity B_{DC} is directly proportional to the D_{TR} , and is unrelated to the FWHM. The best sensitivity is 8.73 pm/Gs for the FOMM with a D_{TR} of 13.5, and is slightly better than the best value of reported microcavity magnetometers^{56,57} which is not applicable to AC magnetic-field measurement due to slow response of magnetic fluid. Notice that the measurable DC magnetic-field range of the FOMM based on Terfenol-D material is ten times larger than that of the microcavity magnetometers using magnetic fluid. This is attributed to the fact that the saturated magnetic intensities of the Terfenol-D material and magnetic fluid are about 2300 Gs and 220 Gs, respectively⁵⁷. The best DC sensitivity of this device is also better than that of typical fiber-optic magnetometers^{58,59}. On the other hand, the AC magnetic-field sensitivity is proportional to the D_{TR} , and is inversely proportional to the FWHM of the PFBG. The best AC sensitivity of 537 fTHz^{1/2} is achieved for the FOMM with FWHM of 1.4 pm and D_{TR} of 5.1. This result is better than the reported values of previous optomechanical magnetometers^{40–45}. The sensitivity of this magnetometer is mainly determined by the magnetostrictive mechanical resonator, PFBG, and deformation transfer ratio. By using a mechanical resonator with larger magnetostrictive coefficient and increasing the deformation transfer ratio, both DC and AC sensitivities can be improved. In addition, the AC sensitivity could be further enhanced by decreasing

the FWHM of the PFBG and increasing the Q_m of the magnetostrictive mechanical resonator.

Methods

Fabrication of the FOMM

The key component of the proposed optomechanical sensor network is the fiber MR. The fiber MR is fabricated by packaging a standard PFBG into two separate silica capillaries with high-hardness adhesive or arc-discharge splicing progress⁵¹. By adjusting the distance between the two silica capillaries and the diameter of the PFBG, the resonant frequency of the fiber MR could be controlled accurately. In our experiments, the diameter of the PFBG is 125 μm , and the inner and outer diameters of the two silica capillaries are 126 and 1000 μm .

Experimental setup for DC magnetic-field measurement

To sense DC magnetic field, an amplified spontaneous emission (ASE) light source with a wavelength range from 1520 nm to 1570 nm is directed to the sensing network through a fiber circulator. The reflective light from the sensing network, which contains the deformation signals from the DC magnetic field, is monitored by an optical spectrum analyzer. By measuring the wavelength shifts of the

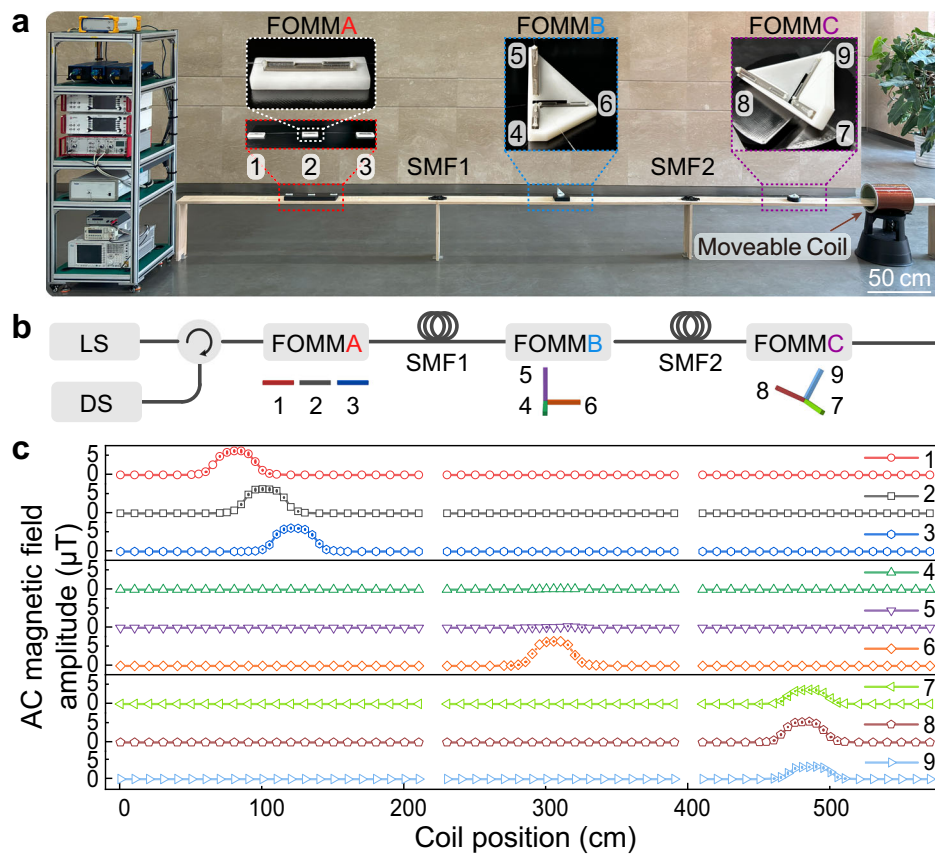


Fig. 4 | Responses of the optomechanical sensor network. **a** Image of the optomechanical sensor network system. **b** Schematic diagram of the optomechanical sensor network system. **c** Responses of the sensor network with nine FOMMs

for the 6.4 μT AC magnetic field at the resonance frequency of the Terfenol-D rod from the coil. *LS* light source, *DS* demodulated system, *SMF1* and *SMF2*: 1-kilometer standard SMF.

PFBG, the DC magnetic field can be demodulated in real time, as shown in Fig. 2. To exclude the unwanted effects of temperature fluctuations, an additional fiber-Bragg grating with different resonant wavelength is cascaded for real-time measurement of ambient temperature.

Experimental setup for AC magnetic-field measurement

The experimental setup for AC magnetic-field measurement is shown in Fig. 1. We use continuously tunable lasers (CTL) to monitor the deformation of the fiber MR, and demodulate the reflective light from the sensing network using balanced amplified photodetector, digital storage oscilloscopes, and electric spectrum analyzers. After obtaining the reflective spectrum of the PFBG, the wavelength of the probe light from the CTL is scanned around the resonant dip of the PFBG to choose a suitable value for the best slope k . The DC component from the photodetector is measured by the digital storage oscilloscope, and could be used to lock the laser to the PFBG. The corresponding AC component of the photodetector is monitored by the electric spectrum analyzer to achieve the power spectral densities of the noise and the response of the sensing network under AC magnetic-field excitation.

Data availability

The data in Figs. 1–4 are provided in the Source Data file. The raw data are available from the corresponding author upon request. Source data are provided with this paper.

Code availability

The codes are available upon request from the corresponding author.

References

- Seng, K. P., Ang, L. M. & Ngharamike, E. Artificial intelligence internet of things: a new paradigm of distributed sensor networks. *Int. J. Distrib. Sens. Netw.* **18**, 15501477211062835 (2022).
- Belhajem, I., Maissa, Y. B. & Tamtaoui, A. Improving vehicle localization in a smart city with low cost sensor networks and support vector machines. *Mob. Netw. Appl.* **23**, 854–863 (2018).
- Nakstad, H. & Kringlebotn, J. T. Oil and gas applications: probing oil fields. *Nat. Photon.* **2**, 147–149 (2008).
- Lindsey, N. J., Dawe, T. C. & Ajo-Franklin, J. B. Illuminating seafloor faults and ocean dynamics with dark fiber distributed acoustic sensing. *Science* **366**, 1103 (2019).
- Li, J. X., Kim, T., Lapusta, N., Biondi, E. & Zhan, Z. W. The break of earthquake asperities imaged by distributed acoustic sensing. *Nature* **620**, 800–806 (2023).
- Jousset, P. et al. Fibre optic distributed acoustic sensing of volcanic events. *Nat. Commun.* **13**, 1753 (2022).
- Aspelmeyer, M., Kippenberg, T. J. & Marquardt, F. Cavity optomechanics. *Rev. Mod. Phys.* **86**, 1391–1452 (2014).
- Hong, S. K. et al. Hanbury brown and twiss interferometry of single phonons from an optomechanical resonator. *Science* **358**, 203–206 (2017).
- Chen, W. J., Kaya Özdemir, Ş., Zhao, G. M., Wiersig, J. & Yang, L. Exceptional points enhance sensing in an optical microcavity. *Nature* **548**, 192–196 (2017).
- Zhang, M. Z. et al. Quantum noise theory of exceptional point amplifying sensors. *Phys. Rev. Lett.* **123**, 180501 (2019).
- Kuang, T. F. et al. Nonlinear multi-frequency phonon lasers with active levitated optomechanics. *Nat. Phys.* **19**, 414–419 (2023).

12. Xia, Y. et al. Entanglement-enhanced optomechanical sensing. *Nat. Photon.* **17**, 470–477 (2023).
13. Koppenhöfer, M. et al. Single-spin readout and quantum sensing using optomechanically induced transparency. *Phys. Rev. Lett.* **130**, 093603 (2023).
14. Wu, N. et al. On-chip mechanical exceptional points based on an optomechanical zipper cavity. *Sci. Adv.* **9**, eabp8892 (2023).
15. Schreppler, S. et al. Optically measuring force near the standard quantum limit. *Science* **344**, 1486–1489 (2014).
16. Mason, D., Chen, J. X., Rossi, M., Tsaturyan, Y. & Schliesser, A. Continuous force and displacement measurement below the standard quantum limit. *Nat. Phys.* **15**, 745–749 (2019).
17. Fogliano, F. et al. Ultrasensitive nano-optomechanical force sensor operated at dilution temperatures. *Nat. Commun.* **12**, 4124 (2021).
18. Allain, P. E. et al. Optomechanical resonating probe for very high frequency sensing of atomic forces. *Nanoscale* **12**, 2939–2945 (2020).
19. Chae, J. et al. Nanophotonic atomic force microscope transducers enable chemical composition and thermal conductivity measurements at the nanoscale. *Nano Lett.* **17**, 5587–5594 (2017).
20. Peano, V., Schwefel, H. G. L., Marquardt, C. H. & Marquardt, F. Intracavity squeezing can enhance quantum-limited optomechanical position detection through deamplification. *Phys. Rev. Lett.* **115**, 243603 (2015).
21. Kampel, N. S. et al. Improving broadband displacement detection with quantum correlations. *Phys. Rev. X* **7**, 021008 (2017).
22. Liu, T. R. et al. Integrated nano-optomechanical displacement sensor with ultrawide optical bandwidth. *Nat. Commun.* **11**, 2407 (2020).
23. Clarke, J., Neveu, P., Khosla, K. E., Verhagen, E. & Vanner, M. R. Cavity quantum optomechanical nonlinearities and position measurement beyond the breakdown of the linearized approximation. *Phys. Rev. Lett.* **131**, 053601 (2023).
24. Kim, P. H. et al. Magnetic actuation and feedback cooling of a cavity optomechanical torque sensor. *Nat. Commun.* **8**, 1355 (2017).
25. Hoang, T. M. et al. Torsional optomechanics of a levitated non-spherical nanoparticle. *Phys. Rev. Lett.* **117**, 123604 (2016).
26. Lai, Y. H. et al. Earth rotation measured by a chip-scale ring laser gyroscope. *Nat. Photon.* **14**, 345–349 (2020).
27. Schliesser, A., Anetsberger, G., Rivière, R., Arcizet, O. & Kippenberg, T. J. High-sensitivity monitoring of micromechanical vibration using optical whispering gallery mode resonators. *N. J. Phys.* **10**, 095015 (2008).
28. Krause, A. G., Winger, M., Blasius, T. D., Lin, Q. & Painter, O. A high-resolution microchip optomechanical accelerometer. *Nat. Photon.* **6**, 768–772 (2012).
29. Guzmán Cervantes, F., Kumanchik, L., Pratt, J. & Taylor, J. M. High sensitivity optomechanical reference accelerometer over 10 kHz. *Appl. Phys. Lett.* **104**, 221111 (2014).
30. Gil-Santos, E. et al. Optomechanical detection of vibration modes of a single bacterium. *Nat. Nanotechnol.* **15**, 469–474 (2020).
31. Tang, S. J. et al. Single-particle photoacoustic vibrational spectroscopy using optical microresonators. *Nat. Photon.* **17**, 951–956 (2023).
32. Westerveld, W. J. et al. Sensitive, small, broadband and scalable optomechanical ultrasound sensor in silicon photonics. *Nat. Photon.* **15**, 341–345 (2021).
33. Basiri-Esfahani, S., Armin, A., Forstner, S. & Bowen, W. P. Precision ultrasound sensing on a chip. *Nat. Commun.* **10**, 132 (2019).
34. Guggenheim, J. A. et al. Ultrasensitive plano-concave optical microresonators for ultrasound sensing. *Nat. Photon.* **11**, 714–719 (2017).
35. Fan, L. R. et al. Superconducting cavity electro-optics: a platform for coherent photon conversion between superconducting and photonic circuits. *Sci. Adv.* **4**, eaar4994 (2018).
36. Bochmann, J., Vainsencher, A., Awschalom, D. D. & Cleland, A. N. Nanomechanical coupling between microwave and optical photons. *Nat. Phys.* **9**, 712–716 (2013).
37. Bagci, T. et al. Optical detection of radio waves through a nano-mechanical transducer. *Nature* **507**, 81–85 (2014).
38. Yoon, T. et al. Simultaneous Brillouin and piezoelectric coupling to a high-frequency bulk acoustic resonator. *Optica* **10**, 110–117 (2023).
39. Jiang, W. T. et al. Optically heralded microwave photon addition. *Nat. Phys.* **19**, 1423–1428 (2023).
40. Forstner, S. et al. Cavity optomechanical magnetometer. *Phys. Rev. Lett.* **108**, 120801 (2012).
41. Yu, C. Q. et al. Optomechanical magnetometry with a macroscopic resonator. *Phys. Rev. Appl.* **5**, 044007 (2016).
42. Colombano, M. F. et al. Ferromagnetic resonance assisted optomechanical magnetometer. *Phys. Rev. Lett.* **125**, 147201 (2020).
43. Li, B. B. et al. Ultrabroadband and sensitive cavity optomechanical magnetometry. *Photonics Res* **8**, 1064–1071 (2020).
44. Xu, A. N., Li, Y. F., Li, X. L., Liu, B. & Liu, Y. C. Subpicotesla optomechanical magnetometry. *Phys. Rev. Lett.* **133**, 153601 (2024).
45. Hu, Z. G. et al. Picotesla-sensitivity microcavity optomechanical magnetometry. *Light.: Sci. Appl.* **13**, 279 (2024).
46. Wu, M. et al. Nanocavity optomechanical torque magnetometry and radiofrequency susceptometry. *Nat. Nanotechnol.* **12**, 127–131 (2017).
47. Yu, W. Y., Jiang, W. C., Lin, Q. & Lu, T. Cavity optomechanical spring sensing of single molecules. *Nat. Commun.* **7**, 12311 (2016).
48. Sansa, M. et al. Optomechanical mass spectrometry. *Nat. Commun.* **11**, 3781 (2020).
49. Lamberti, F. R. et al. Real-time sensing with multiplexed optomechanical resonators. *Nano Lett.* **22**, 1866–1873 (2022).
50. Monerie, M. & Jeunhomme, L. Polarization mode coupling in long single-mode fibres. *Opt. Quantum Electron.* **12**, 449–461 (1980).
51. Zhang, Q., Zhai, R. L., Yang, S. W., Yang, S. & Li, Y. M. Microfiber mechanical resonator for optomechanics. *ACS Photonics* **7**, 695–700 (2020).
52. Gagliardi, G., Salza, M., Avino, S., Ferraro, P. & Natale, P. D. Probing the ultimate limit of fiber-optic strain sensing. *Science* **330**, 1081–1084 (2010).
53. Fagaly, R. L. Superconducting quantum interference device instruments and applications. *Rev. Sci. Instrum.* **77**, 101101 (2006).
54. Kellogg, R. & Flatau, A. Wide band tunable mechanical resonator employing the ΔE effect of terfenol-D. *J. Intell. Mater. Syst. Struct.* **15**, 355–368 (2004).
55. Hathaway, K. B., Clark, A. E. & Teter, J. P. Magnetomechanical damping in giant magnetostriction alloys. *Metall. Mater. Trans. A* **26**, 2797–2801 (1995).
56. Zhu, S., Shi, L., Liu, N. Y., Xu, X. B. & Zhang, X. L. Magnetic field sensing using magnetic-fluid-filled optofluidic ring resonator. *Microfluid. Nanofluid.* **21**, 156 (2017).
57. Zhao, X. Y. et al. Research on magnetic field sensing based on whispering gallery modes microbubble resonator. *Sci. Sin. -Phys. Mech. Astron.* **53**, 114208 (2023).
58. Rostami, A. et al. Advances in fibre Bragg grating technology for magnetic field sensing: a review. *Measurement* **221**, 113482 (2023).
59. Zhan, B. Y. et al. Terfenol-d based magnetic field sensor with temperature independence incorporating dual fiber Bragg gratings structure. *IEEE Access* **9**, 32713–32720 (2021).

Acknowledgements

We thank Shangran Xie, Chang-Ling Zou, Beibei Li, and Jie Li for helpful discussions. This work is supported by: National Natural Science Foundation of China (grants no. 12174232, 12222409, U21A6006 and 11804208), Innovation Program for Quantum Science and Technology (grants no. 2023ZD0300400), the Fundamental Research Program of Shanxi Province (202203021223001).

Author contributions

S.Y., Q.Z., H.S., and Y.L. conceived and designed the experiments. S.Y., Q.Z., and L.Y. performed the experiments. S.Y., Q.W., H.L., and P.Z. analyzed the data. S.Y., Q.Z., H.S., and Y.L. wrote the manuscript with input from all authors. Q.Z., H.S., and Y.L. supervised this work. All authors discussed the results and commented on the manuscript.

Competing interests

The authors declare no competing interests.

Additional information

Supplementary information The online version contains supplementary material available at <https://doi.org/10.1038/s41467-025-66350-2>.

Correspondence and requests for materials should be addressed to Qiang Zhang, Heng Shen or Yongmin Li.

Peer review information *Nature Communications* thanks the anonymous reviewer(s) for their contribution to the peer review of this work. A peer review file is available.

Reprints and permissions information is available at <http://www.nature.com/reprints>

Publisher's note Springer Nature remains neutral with regard to jurisdictional claims in published maps and institutional affiliations.

Open Access This article is licensed under a Creative Commons Attribution-NonCommercial-NoDerivatives 4.0 International License, which permits any non-commercial use, sharing, distribution and reproduction in any medium or format, as long as you give appropriate credit to the original author(s) and the source, provide a link to the Creative Commons licence, and indicate if you modified the licensed material. You do not have permission under this licence to share adapted material derived from this article or parts of it. The images or other third party material in this article are included in the article's Creative Commons licence, unless indicated otherwise in a credit line to the material. If material is not included in the article's Creative Commons licence and your intended use is not permitted by statutory regulation or exceeds the permitted use, you will need to obtain permission directly from the copyright holder. To view a copy of this licence, visit <http://creativecommons.org/licenses/by-nc-nd/4.0/>.

© The Author(s) 2025